IGARSS 2024 - 2024 IEEE International Geoscience and Remote Sensing Symposium | 979-8-3503-6032-5/24/$31.00 ©2024 IEEE | DOI: 10.1109/IGARSS53475.2024.10640448

A MULTI-CHANNEL AIRBORNE UHF RADAR SOUNDER SYSTEM FOR OLDEST ICE EXPLORATION: DEVELOPMENT AND DATA COLLECTION

S. Kaundinya, J. Paden, S. Jacob, C. Shupert, B. Schroeder, R. Hale, E. Arnold, U. Dey Sarkar, V. Occhiogrosso, L. Taylor, S. McMillan, and F. Rodriguez-Morales

Center for Remote Sensing and Integrated Systems, University of Kansas, USA

ABSTRACT

The Center for Oldest Ice Exploration (COLDEX) project is exploring Antarctica to find a continuous ice record from the present to 1.5 million years ago and document the mid-Pleistocene transition, which occurred ~1 million years ago. The current longest ice record is 800,000 years old. This work describes a new 600-900 MHz UHF radar to help address this challenge with a 1) much larger, 22.8 m or 57-wavelength, cross-track antenna array and 2) higher transmit power, than prior renditions. Survey flights on a Basler aircraft were conducted from the South Pole in 2022-2023 and in 2023-2024. In this work, we provide an overview of the design requirements, the radar system architecture, and antenna array implementation. We also present preliminary results from aerial surveys conducted in Antarctica.

Index Terms— UHF ice-penetrating radar, oldest ice, COLDEX.

1. INTRODUCTION

Due to the nature of snow accumulation and compaction and the entrapment of atmospheric particles with seasonal accumulation, ice sheets can be regarded as layered media with each layer being an isochrone. The layers form over large areas during temporally constrained events (*e.g.* due to volcanic material precipitating out of the atmosphere during a period of increased volcanism) [1]. Layer boundaries may be detected by a radar due to scattering, and if a layer can be traced from a location where the ice has been dated to the radar survey region (*e.g.* from a previous ice core drilling project), the age of the ice at the depth of the layer will be known wherever that layer is detectable.

Ice layer stratigraphy is generally coherent from one year to the next if the spatial baseline between passes is small enough [2]. Using interferometric techniques, the downward vertical velocity of the ice layers can be precisely measured by interfering the phases after coregistering the layers from the two passes and compensating for the spatial baseline. The age of the ice, assuming steady state velocity fields, can then be estimated by integrating the vertical velocity. Vertical velocity estimates from an airborne platform require estimates of cross-track slopes to compensate for the spatial baseline [2]. In addition, ice is known to fold and sheer at depth, which can result in temporally discontinuous layers [3]. Three-dimensional radar imaging eases interpretation of folding and sheering features by providing cross- and along-track layer slope measurements as well as ice bed topography maps to infer ice flow anomalies that may disturb the internal stratigraphy [4].

Science-driven requirements pointed us towards a radar system with a wide bandwidth for layer tracing and a very large cross-track antenna aperture to achieve sufficient elevation angular resolution and estimating cross-track layer slope and ice bed topography. The radar described in this work was developed to augment the existing University of Texas Institute for Geophysics (UTIG) instrument suite, which includes a 60 MHz VHF antenna [5]. We chose 600-900 MHz because it provides ~0.5 m resolution in ice, which we know to be sufficient to resolve most layering from the surface to the bottom and it extends existing 600-900 MHz datasets [6]. UHF radar signals also enable a very fine beamwidth (<1 deg). Since the VHF radar from UTIG already includes one large antenna per wing, our work focused on instrumenting the fuselage and the wings inboard and outboard of the VHF antennas. To accelerate radar development and aircraft certification process, we retrofitted an existing Basler fuselage fairing [7] in the first year. In the second year, we developed a smaller and lighter-weight wing antenna fairing that could be individually placed along the wing. In this paper, we provide an overview of the instrument design, implementation, field operation and sample results.

2. SYSTEM OVERVIEW

2.1. Radar electronics

We housed the radar system in three separate chassis. The two primary chassis are interchangeable and include DC-power conditioning circuitry, a digital module (OnLogic Linux PC and Arena 522 from Tomorrow.io), clock generation and distribution circuitry, a GNSS receiver connected to an external inertial measurement unit (IMU), a 4-channel high-power transmitter, and an 8-channel analog receiver bank (Fig. 1). Chassis 3 contains just the DC circuitry, digital module and 8-channel analog receiver bank. The Arena 522 modules are based on the Xilinx's 3rd generation ZU47DR RF system-on-chip (RFSoC) devices.

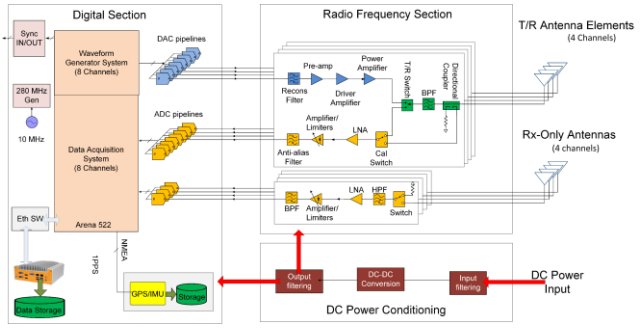

Fig 1. Simplified block diagram of the primary chassis.

These modules have eight 14-bit analog-to-digital (ADC) channels with a maximum sampling rate of 5 GSPS; eight digital-to-analog-converter (DAC) pipelines with 14-bit resolution and a maximum sampling rate of 9.85 GSPS; programmable logic and a multiple-core CPU. We use a 10 MHz OCXO and generate 280-MHz from this; both are used by the digital modules for sampling. The Arena 522 only have 4kS per channel for waveform capture and are limited to 70 MSPS IQ-sampling since the current digital design for our radar system is still incomplete (300 MSPS IQ and deep memory). The ADC samples at 4480 MSPS and the digital system decimates to the maximum recording rate of 70 MSPS. The DAC samples at 8960 MSPS and uses a programmable DDS to generate chirps with phase, delay, and amplitude control.

The high-power transmitter channels filter and amplify the signals from four of the DACs using a multi-stage RF amplifier chain with a 3-dB compression point of 61.2 dBm (1318 W) at 725 MHz. Although the target power level at the output of the PA was 62.04 dBm (1,600 W) per channel, we operated at about 59.04 dBm at the output of the PA (800 W). The outputs of the power amplifiers (PA) go through a bank of transmit/receive switches, band-pass filters and bi-directional couplers before being applied to the transmit/receive antennas. The signals from the receive ports of the T/R switches as well as four extra signals from a set of four receive-only antennas, are applied to a bank of de-compression-based receivers, like those in [8]. The receiver outputs are captured by eight ADC pipelines and recorded onto a USB 3.0 SSD at a rate of 70 MB/s. All digital components are connected via Ethernet and controlled remotely through virtual network computing (VNC) session.

2.2. Antenna array

The antenna array, shown in Fig. 2, consists of a fuselage fairing with 64 dual-polarized antennas arranged in a 4 x 16 grid and three wing fairings placed on each wing, where each fairing has 4 single-polarization antennas arranged in a 2x2 grid. Custom-designed Wilkinson RF power combiners feed each column of four fuselage elements so that there are sixteen dual-polarized channels presented to the radar. Similar circuits combine the 2x2 wing elements presenting six wing-channels to the radar. A set of lumped-element passive networks is used to improve impedance matching.

Fig. 2. Fuselage and wing antenna arrays photo/models.

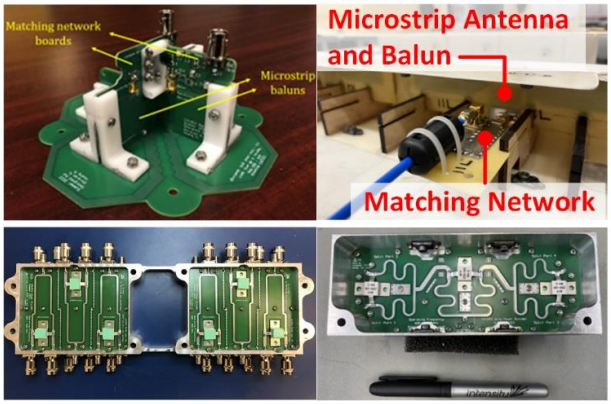

Fig. 3: Fuselage antenna (top left) and power divider (bottom left); wing antenna (top right) and power divider (bottom right).

The primary challenge of the fuselage array implementation was adapting the electrical design to fit the existing fairing, which could only be minimally modified, resulting in un-optimizable antenna spacings and a space-constrained power divider design. Each element of the fuselage fairing is a microstrip dual-polarized dipole antenna fed by microstrip aperture-coupled baluns and microstrip lumped-element matching networks [9], as shown in Fig. 3. It is designed to be operated in the 600-900 MHz band, but the resulting return loss was higher than desired at certain frequencies, reaching up to 6 dB. This was due to the input reflection characteristics of the RF power divider and related to the parasitic capacitance and mechanical integration effects of the flange-mount isolation resistors (100 Ω, 250 W) selected for high-power operation.

In contrast, the design of the wing fairings is new, and the structure was adapted around the electrical design. Each single-polarization antenna is a microstrip dipole with a surface-mount balun (capable of high-power operation) and a lumped-element impedance matching network. The along-track spacing is 20.5 cm and the cross-track spacing is 21 cm. All four antennas are power combined with a custom-designed circuit made to fit into the pylon. We used ferrite cores installed near the antenna and on the sum port of the RF power combiner to minimize unwanted common mode currents on the coaxial cables. We implemented a lower-power design for the power combiner that works over the full 300-MHz bandwidth, though currently these channels are only be used for reception based on the backend design.

The eight independently controlled transmit channels discussed in Section 2.1 allow transmit beam forming and transmit phase center diversity, but the aircraft DC power configuration (one 28 V, 70 A bus for the transmitters) limits simultaneous full power transmission to four channels at 10% duty cycle. The receive gain of the digitally beam formed 64-element fuselage array is ~21 dB. The nadir gain from four channels in the fuselage array (16-elements) is ~15 dB. The wing antenna gain is 10.6 dB at 750 MHz.

3. AIRCRAFT INTEGRATION AND FIELD OPERATIONS

The radar was integrated onto a Basler aircraft as part of COLDEX and was used in two field surveys. The system has collected 25 TB of data over 15,000 line-km of data as of the time of writing. Fig. 4 shows a map of the flightlines. Typical field operations include one or two 5-hour flights per day (driven by the weight of the instrument suite, skied operations, and the high altitude at takeoff). We use a custom pilot navigation system to achieve high trajectory accuracy (5-10 m) during the survey to improve multi-pass results.

Fig. 5a shows a photograph of the instrumented aircraft at South Pole during the current 2023-2024 campaign marking the various radar antenna fairings. Fig. 5b shows the cabin instrument rack installation. A custom pulse sequencing interface sent via CAT-6 cables and shared 10-MHz and 280 MHZ clocks (discussed in Section 2.1) provides synchronization between chassis. The transmit events of the UTIG VHF radar and the UHF radar are made concurrent to keep feedthrough noise away from the time-window set for capturing deeper layers and ice bottom, where maximum sensitivity is required. To achieve this, the 10 MHz clock signal is provided by the VHF radar and the UHF transmit pulse sequence is initiated off the enable signal for the VHF power amplifier. Coherent noise from switching events is mitigated via zero-pi inter-pulse modulation.

4. INITIAL RESULTS

We conducted flights over smooth sea ice and ocean water for system calibration. During calibration routines, the radar

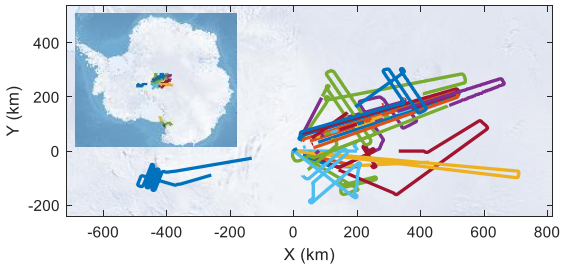

Fig. 4. Flight line map around South Pole (map origin) in polar stereographic projection; the inset shows the location in the context of Antarctica.

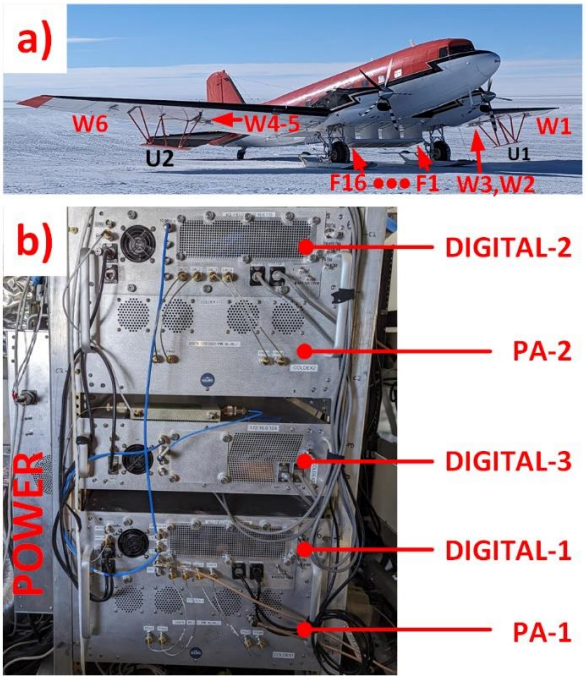

Fig. 5. a) Photograph of the instrumented Basler aircraft at the South Pole. The six UHF wing antenna fairings are indicated as W1 - W6, the UTIG VHF radar fairings are marked as U1-U2, and the fuselage fairing channels are labelled as F1-F16. b) Photograph of the instrument rack with the three chassis inside the plane. The primary chassis 1-2 are partitioned into digital (top) and high-power transmitters (bottom) with power amplifier (PA) sections. The receive-only chassis 3 is marked as "Digital 3" and includes a bank of eight analog receivers and no transmitters.

cycles through eight different modes with one transmitter being excited per mode so that the performance of each transmitter can be isolated, while the 22 receivers record the radar returns. The aircraft flies straight and level for the first part of the calibration routine to obtain the impulse response from the system and equalize the transmitters and receivers in the broadside (nadir) direction. The system response measured from a quasi-specular sea ice lead (red) is shown in Fig. 6 along with the ideal impulse response (black).

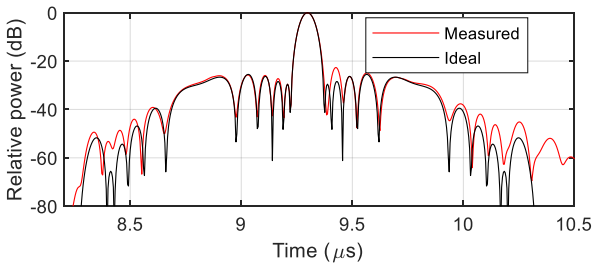

Fig. 6. Ideal and in-flight measured system impulse response.

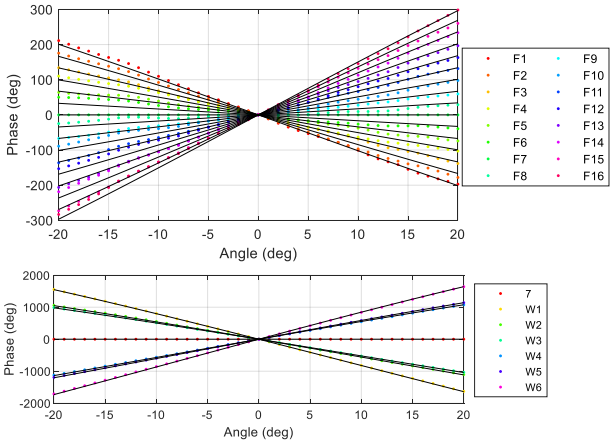

Fig. 7. Points show in-flight measured phases for fuselage antennas (top) and wing antennas relative to antenna F7 (bottom). The straight lines show the ideal phase based on antenna positions derived from spatial surveys and computer models. Mean phase deviation from ideal is 12°.

Equalization removes time delay offsets between the channels as well as the relative phase offset between channels. Next, the aircraft rolls side-to-side ±20 deg at about one degree of roll per second. The relative amplitude and phase between a reference channel (7) and each receiver is then estimated for each roll angle to build a steering vector table for direction of arrival analysis. Fig. 7 shows the resulting steering vector patterns. Phase deviations are asymmetric and largest (~40°) for the tightly spaced elements likely due to asymmetric fairing structures and mutual coupling respectively. Deviations from ideal are important to compensate for in direction of arrival processing to achieve optimal 3D images and elevation angle estimates [10]. The amplitudes (not shown) are nearly isotropic over this angular range, varying by only ±1.25 dB.

Fig. 8 is an example survey image from data acquired near the South Pole. After combining the signals from the sixteen fuselage channels, the ice bottom is barely discernible underneath the blue line at ~2.75 km depth. In some areas, due to signal extinction [1], the bed is detected with low signal-to-noise ratio or not detectable. This confirms the suitability of lower frequencies for bed imaging in deep ice [6-7],[10]. While some increase in transmit power is possible, the UHF radar is operating near the limits of the available aircraft power. Internal layers are detectable through most of the ice column and the preliminary cross-track slope accuracy achieved using uncalibrated steering vectors is ~0.5 degrees.

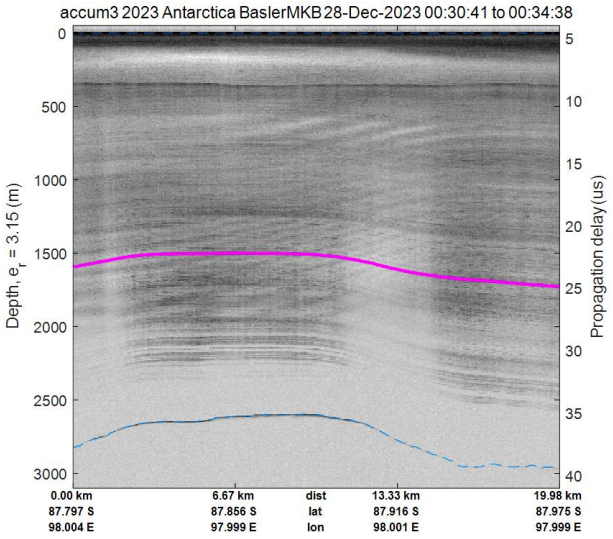

Fig. 8. Sample radar echogram showing surface (0 m depth) and bottom (~2750+ m depth) in blue, and an example internal layer tracked in magenta.

5. ACKNOWLEDGEMENT

Funding was provided by the National Science Foundation Center for OLDest Ice Exploration (COLDEX) project (OPP-2019719). We gratefully acknowledge our CReSIS affiliates, support from UTIG and the aircraft crews, and Mr. J. Sonntag for providing the navigation system.

6. REFERENCES

[1] S. Fujita, *et al.*, A summary of the complex dielectric permittivity of ice in the megahertz range and its application for radar sounding of polar ice sheets, *Physics of Ice Core Records*, Edited by T. Hondoh, Hokkaido University Press, 2000, Sapporo, pp. 185-212.

[2] G. Ariho, *et al.*, Joint Estimation of Ice Sheet Vertical Velocity and Englacial Layer Geometry from Multipass Synthetic Aperture Radar Data, *Proc. 2022 IEEE Int. Symp. Phased Array Syst. & Tech.*, Oct. 2022.

[3] Dorthe Dahl-Jensen *et. al.*, "Eemian interglacial reconstructed from folded NEEM ice core strata," *Nature*, vol. 493, pp. 489-494, Jan. 2013.

[4] J. Paden, *et al.*, Ice-sheet bed 3-D tomography, *J. Glaciol.* 2010; 56 (195): 3-11. doi:10.3189/002214310791190811.

[5] Online: https://www-udc.ig.utexas.edu/external/facilities/aero/

[6] E. Arnold, *et al.*, CReSIS airborne radars and platforms for ice and snow sounding. *Ann. Glaciol.*, 61, no. 81 (2020): 58-67.

[7] R. Hale *et al.*, Multi-channel Ultra-wideband radar sounder and imager, *Proc. 2016 IEEE Int. Geosci. Remote Sens. Symp.*, Jul. 2016, pp. 2112-2115.

[8] U. Dey Sarkar, *et al.*, Decompression-Based Receiver Design for Radar Ice Sounding Applications, *Proc. 2023 IEEE Int.Geosci. Remote Sens. Symp.*, pp. 211-214.

[9] H. Mai and F. Rodriguez-Morales, Broadband Dual- Polarized Planar Antennas for Radar with Printed Circuit Balun, *Proc. 2021 ICRAMET*, Nov. 2021, pp. 89-94.

[10] T. Moore, *et al.*, Nonparametric array manifold calibration for ice sheet tomography, *IEEE TGRS,* Vol. 60, 2022, pp. 4303520.